

# RHESSI and SOHO/CDS Observations of Explosive Chromospheric Evaporation

Ryan O. Milligan<sup>1,3</sup>, Peter T. Gallagher<sup>2,3,4</sup>, Mihalios Mathioudakis<sup>1</sup>, D. Shaun Bloomfield<sup>1</sup>, Francis P. Keenan<sup>1</sup>, and Richard A. Schwartz<sup>3,5</sup>

## ABSTRACT

Simultaneous observations of explosive chromospheric evaporation are presented using data from the *Reuven Ramaty High Energy Solar Spectroscopic Imager (RHESSI)* and the Coronal Diagnostic Spectrometer (CDS) onboard *SOHO*. For the first time, co-spatial imaging and spectroscopy have been used to observe explosive evaporation within a hard X-ray emitting region. *RHESSI* X-ray images and spectra were used to determine the flux of non-thermal electrons accelerated during the impulsive phase of an M2.2 flare. Assuming a thick-target model, the injected electron spectrum was found to have a spectral index of  $\sim 7.3$ , a low energy cut-off of  $\sim 20$  keV, and a resulting flux of  $\geq 4 \times 10^{10}$  ergs cm<sup>-2</sup> s<sup>-1</sup>. The dynamic response of the atmosphere was determined using CDS spectra, finding a mean upflow velocity of  $230 \pm 38$  km s<sup>-1</sup> in Fe XIX (592.23 Å), and associated downflows of  $36 \pm 16$  km s<sup>-1</sup> and  $43 \pm 22$  km s<sup>-1</sup> at chromospheric and transition region temperatures, respectively, relative to an averaged quiet-Sun spectra. The errors represent a  $1\sigma$  dispersion. The properties of the accelerated electron spectrum and the corresponding evaporative velocities were found to be consistent with the predictions of theory.

*Subject headings:* Sun: atmospheric motions – Sun: flares – Sun: UV radiation – Sun: X-rays,  $\gamma$  rays

## 1. INTRODUCTION

Current solar flare models (Antiochos & Sturrock 1978; Fisher, Canfield, & McClymont 1984, 1985a,b,c; Mariska, Emslie, & Li 1989) predict two types of chromospheric evaporation processes. “Gentle” evaporation occurs when the chromosphere is heated either directly by non-thermal electrons, or indirectly by thermal conduction. The chromospheric plasma subsequently loses energy via a combination of radiation and low-velocity hydrodynamic expansion. “Explosive” evaporation takes place when the chromosphere is

unable to radiate energy at a sufficient rate and consequently expands at high velocities into the overlying flare loops. The overpressure of evaporated material also drives low-velocity downward motions into the underlying chromosphere, in a process known as chromospheric condensation.

From a theoretical perspective, Fisher, Canfield, & McClymont (1985a) investigated the relationship between the flux of non-thermal electrons ( $F$ ) and the velocity response of the atmosphere for the two classes of evaporation. For gentle evaporation, non-thermal electron fluxes of  $\leq 10^{10}$  ergs cm<sup>-2</sup> s<sup>-1</sup> were found to produce upflow velocities of tens of kilometres per second. In contrast, explosive evaporation was found to be associated with higher non-thermal electron fluxes ( $F \geq 3 \times 10^{10}$  ergs cm<sup>-2</sup> s<sup>-1</sup>) which drive both upflows of hot material at velocities of several hundred kilometres per second *and* downflows of cooler material at tens of kilometres per second.

Observationally, previous studies have identified blue-shifted Soft X-Ray and EUV lines indica-

<sup>1</sup>Department of Physics and Astronomy, Queen’s University Belfast, Belfast, BT7 1NN, Northern Ireland.

<sup>2</sup>School of Physics, Trinity College Dublin, Dublin 2, Ireland.

<sup>3</sup>Laboratory for Astronomy and Solar Physics, NASA Goddard Space Flight Center, Greenbelt, MD 20771, U.S.A.

<sup>4</sup>L-3 Communications GSI.

<sup>5</sup>Science Systems and Applications, Inc.

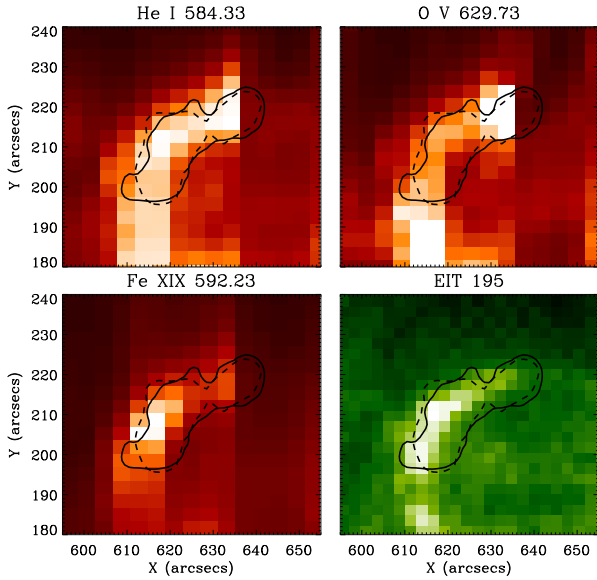


Fig. 1.— CDS images in the He I, O V, and Fe XIX emission lines observed during the impulsive phase of the flare, with the corresponding EIT 195 Å image. *RHESSI* 12–25 keV (*dashed*) and 25–60 keV (*solid*) contours are overlaid, each drawn at 10% of the peak intensity.

tive of chromospheric evaporation. Using the Bent Crystal Spectrometer onboard the *Solar Maximum Mission*, Antonucci & Dennis (1983) and Zarro & Lemen (1988) reported upflow velocities of  $400 \text{ km s}^{-1}$  and  $350 \text{ km s}^{-1}$ , respectively, in Ca XIX lines ( $3.1\text{--}3.2 \text{ Å}$ ). More recently, Czakowska et al. (1999), Teriaca et al. (2003), and Del Zanna et al. (2005) observed velocities of  $140\text{--}200 \text{ km s}^{-1}$  in Fe XIX ( $592.23 \text{ Å}$ ), using the Coronal Diagnostic Spectrometer (CDS; Harrison et al. 1995) onboard the *Solar and Heliospheric Observatory* (SOHO). Simultaneous upflows and downflows during a Hard X-Ray (HXR) burst indicative of explosive evaporation have been observed using CDS and *Yohkoh*/Hard X-Ray Telescope by Brosius & Phillips (2004). While these studies provided a measurement of the dynamic response of the flaring chromosphere, they were unable to provide a measurement of the flux of electrons responsible for driving such motions, nor the spatial relationship between the two.

In this *Letter*, simultaneous *Reuven Ramaty High Energy Solar Spectroscopic Imager* (*RHESSI*;

Lin et al. 2002) and CDS observations are combined for the first time to investigate the relationship between the non-thermal electron flux and the response of the solar atmosphere. In Section 2 the analysis techniques employed are described, while the results are presented in Section 3. Our Conclusions are then given in Section 4.

## 2. OBSERVATIONS AND DATA ANALYSIS

This study focuses on a *GOES* M2.2 flare, which began at 12:44 UT on 2003 June 10. The event was selected from a sample of approximately 50 flares jointly observed by *RHESSI* and CDS. The limited field of view, cadence, and operating schedule of CDS, coupled with *RHESSI* nighttime and South Atlantic Anomaly passes, make simultaneous observations by the two instruments quite rare.

### 2.1. The Coronal Diagnostic Spectrometer (CDS)

The CDS observations reported here were obtained with the *FLARE\_AR* observing sequence. *FLARE\_AR* contains five  $\lesssim 4 \text{ Å}$  wide spectral windows centered on He I ( $584.33 \text{ Å}$ ;  $\log T = 4.5$ ), O V ( $629.73 \text{ Å}$ ;  $\log T = 5.4$ ), Mg X ( $624.94 \text{ Å}$ ;  $\log T = 6.1$ ), Fe XVI ( $360.76 \text{ Å}$ ;  $\log T = 6.4$ ), and Fe XIX ( $592.23 \text{ Å}$ ;  $\log T = 6.9$ ). Each raster consists of 45 slit positions, each  $\sim 15$  seconds long, resulting in an effective cadence of  $\sim 11$  minutes. The slit itself is  $4'' \times 180''$  yielding a  $\sim 180'' \times 180''$  field of view. A zoomed-in region of the He I, O V, and Fe XIX rasters from the impulsive phase of the flare is given in Figure 1. Also shown is the Extreme ultraviolet Imaging Telescope (EIT; Delaboudinière et al. 1995) 195 Å passband image obtained at 12:48 UT. A series of subsequent EIT images makes it clear that the He I and O V brightenings come from a flare ribbon rather than two distinct footpoints as Figure 1 may suggest.

The spectrum from each CDS pixel was fitted with a broadened Gaussian profile (Thompson 1999), for each of the five spectral windows. Velocity maps were created by measuring Doppler shifts relative to quiet-Sun spectra, which were assumed to be emitted by stationary plasma. Preliminary fits to the Fe XIX line during the impulsive phase of the flare revealed an asymmetric broadening beyond the instrumental resolution of

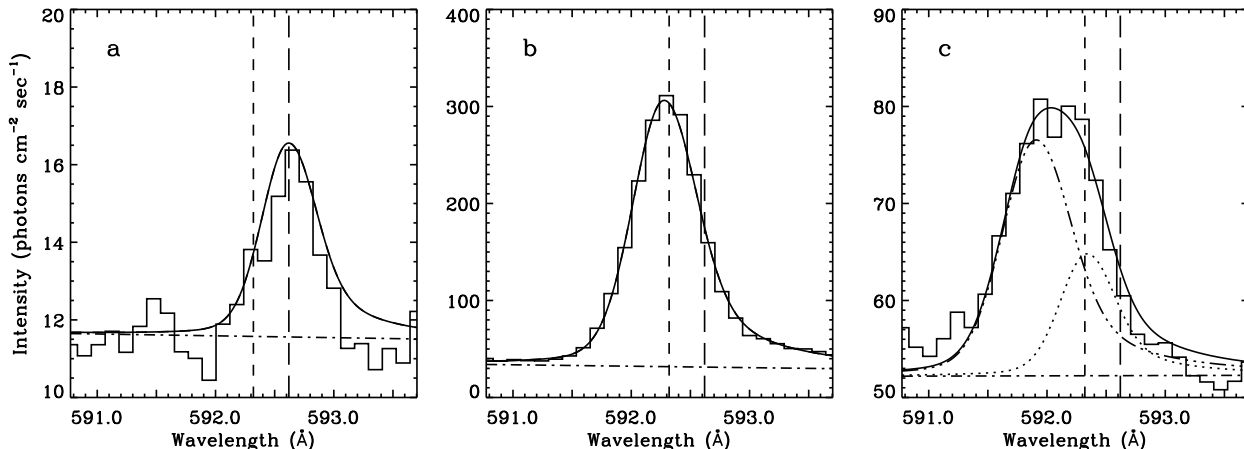


Fig. 2.— Sample of spectra from the spectral window centered on Fe XIX (592.23 Å). The vertical *short-dashed* line shows the rest wavelength of the Fe XIX line at 592.32 Å while the *long-dashed* line shows the rest wavelength of the Fe XII line at 592.62 Å. Panel ‘a’ was obtained from a quiet Sun region, panel ‘b’ shows a stationary Fe XIX line from a post-impulsive phase flare kernel, while panel ‘c’ shows an Fe XIX line from the flare ribbon during the impulsive phase. The *dotted* line indicates the stationary component while the *triple-dot-dashed* line indicates the blue-shifted component.

CDS. The strongest blue asymmetries were found within the flare ribbon during the impulsive phase. Outside this area, and after the impulsive phase, the Fe XIX line was observed to have a width comparable to the instrumental width. Figure 2 shows a sample of spectra taken from the spectral window centered on the Fe XIX (592.23 Å) emission line. Panel ‘a’ shows a spectrum from a quiet Sun area in which no Fe XIX emission was visible. Instead, a weak emission line was observed at 592.6 Å which Del Zanna & Mason (2005) have identified as Fe XII. Panel ‘b’ shows a stationary Fe XIX emission line extracted from a bright region, but after the impulsive phase at  $\sim 12:50$  UT when no significant flows are expected. An emission line with a strong blue asymmetry is shown in panel ‘c’. This was extracted from the flare ribbon during the impulsive phase. The best fit to this line was consistent with stationary and blue-shifted components, both with widths comparable to the instrumental resolution. As Fe XIX is not observed in quiet-Sun spectra, and following from Teriaca et al. (2003), the Doppler velocity was measured as the shift between these two components. A heliographic correction was also applied, due to the longitude of the observations and assuming purely radial flows,

## 2.2. The Reuven Ramaty High Energy Spectroscopic Imager (RHESSI)

*RHESSI* is an imaging spectrometer capable of observing X- and  $\gamma$ -ray emission over a wide range of energies ( $\sim 3$  keV–17 MeV). During this event the thin attenuators on *RHESSI* were in place thus limiting the energy range to  $\gtrsim 6$  keV. Flare emission was not observed above  $\sim 60$  keV. The flare lightcurves are shown in the top panel of Figure 3. Both the *RHESSI* images and spectra were obtained over a 64 second period from 12:47:34–12:48:38 UT to coincide with the timerange over which CDS observed blue asymmetries in the Fe XIX line. This time interval lies within the impulsive 25–60 keV HXR burst and is indicated by two vertical dotted lines in the top panel of Figure 3. *RHESSI* images in two energy bands (12–25 and 25–60 keV) were reconstructed using the *Pixon* algorithm (Hurford et al. 2002). Contours at 10% of the peak intensity in each band are overlaid on each EUV image in Figure 1.

The *RHESSI* spectrum was fitted assuming an isothermal distribution at low energies, and thick-target emission at higher energies (bottom panel of Figure 3). A thick-target model was chosen over a thin-target model as it is believed that the den-

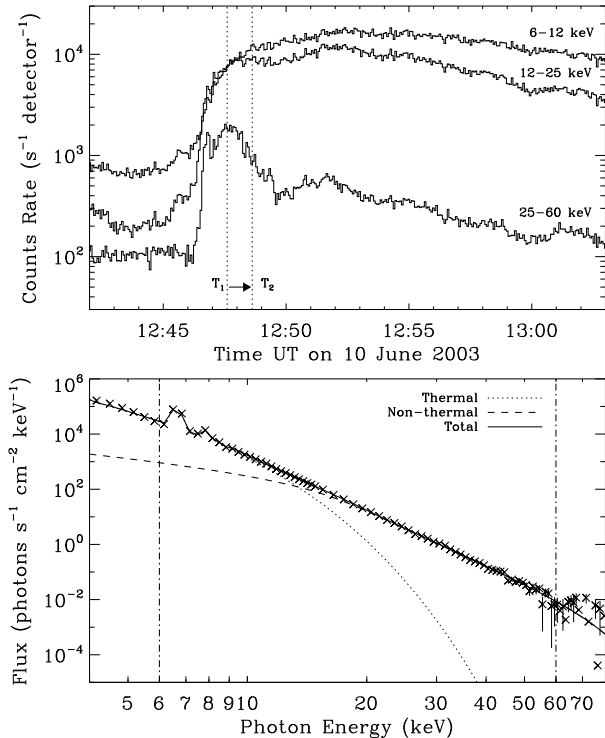


Fig. 3.— *Top panel:* *RHESSI* lightcurves from the 6–12, 12–25, and 25–60 keV bands. The *dotted* vertical lines indicate the time interval over which images and spectra were obtained to correspond to time when significant upflows were observed using CDS. *Bottom panel:* Portion of the *RHESSI* spectrum integrated over the timerange given above. The energy range 6–60 keV (vertical *dot-dash* lines) was fitted with an isothermal component (*dotted curve*) and a thick-target bremsstrahlung component (*dashed curve*).

sity of the flare loop is insufficient to thermalise the electrons as they propagate to the chromosphere. The thick-target model is used in the vast majority of cases (e.g. Holman 2003, Veronig et al. 2005). Furthermore, in this flare the HXR source is clearly aligned with the He I ribbon as seen by CDS, which implies that the accelerated electrons are losing their energy in the dense chromosphere rather than in the coronal loops. The total power of non-thermal electrons above the low energy cut-off ( $\epsilon_c$ ) was calculated from  $P(\epsilon \geq \epsilon_c) = \int_{\epsilon_c}^{\infty} f_e(\epsilon) d\epsilon$  ergs s<sup>-1</sup>, where  $f_e(\epsilon) \sim$

$\epsilon^{-\delta}$  electrons keV<sup>-1</sup> s<sup>-1</sup> is the thick-target electron injection spectrum and  $\delta$  is the associated spectral index (Brown 1971). Because of the steepness of the *RHESSI* spectrum at high energies, the non-thermal flux is quite sensitive to the value of the low energy cut-off. In order to put a constraint on this value, the temperature of the thermal component was obtained by another independent method, i.e. the equivalent width of the Fe line complex at 6.7 keV (Phillips 2004). The value of the equivalent width of this line, which is quite sensitive to the temperature, was used to estimate the temperature of the thermal component. Having fixed this value, the entire *RHESSI* spectrum was fitted using a least-squares fit.

### 3. RESULTS

The thick-target model fitted to the *RHESSI* spectrum in Figure 3 was consistent with an electron distribution having  $\epsilon_c \sim 20$  keV and  $\delta \sim 7.3$ . The break energy of 20 keV is consistent with earlier works (e.g. Holman 2003, Sui, Holman, & Dennis 2005). The total power in non-thermal electrons was therefore  $1 \times 10^{29}$  ergs s<sup>-1</sup>. Exploring the possible range of values for the break energy for this flare would yield an electron power value of  $4 \times 10^{29}$  ergs s<sup>-1</sup> for  $\epsilon_c = 15.0$  keV while  $\epsilon_c = 25.0$  keV would give a power value of  $6 \times 10^{28}$  ergs s<sup>-1</sup>. However, either of these break energies would give a worse  $\chi^2$  value than obtained from the original fit. By comparison, the total thermal power for the same time interval was found to be  $1.2 \times 10^{28}$  ergs s<sup>-1</sup>.

Using the reconstructed 25–60 keV image, an upper-limit to source size was calculated to be  $2.3 \times 10^{18}$  cm<sup>2</sup>. This was found by summing over all pixels with counts greater than 10% of the peak value. This threshold was chosen to eliminate sources outside of the main HXR-emitting region, which were assumed to be unreal; the source area was not found to be highly sensitive to this value. For example, a threshold of 5% yielded an area of  $3.2 \times 10^{18}$  cm<sup>2</sup> and 15% yielded  $2 \times 10^{18}$  cm<sup>2</sup>. This area was also confirmed using the Fourier modulation profiles from each of *RHESSI*'s nine detectors, which are sensitive to spatial scales from 2.2'' to 183''. Assuming a filling factor of unity, the resulting non-thermal electron flux was calculated to be  $\geq 4 \times 10^{10}$  ergs cm<sup>-2</sup> s<sup>-1</sup>.

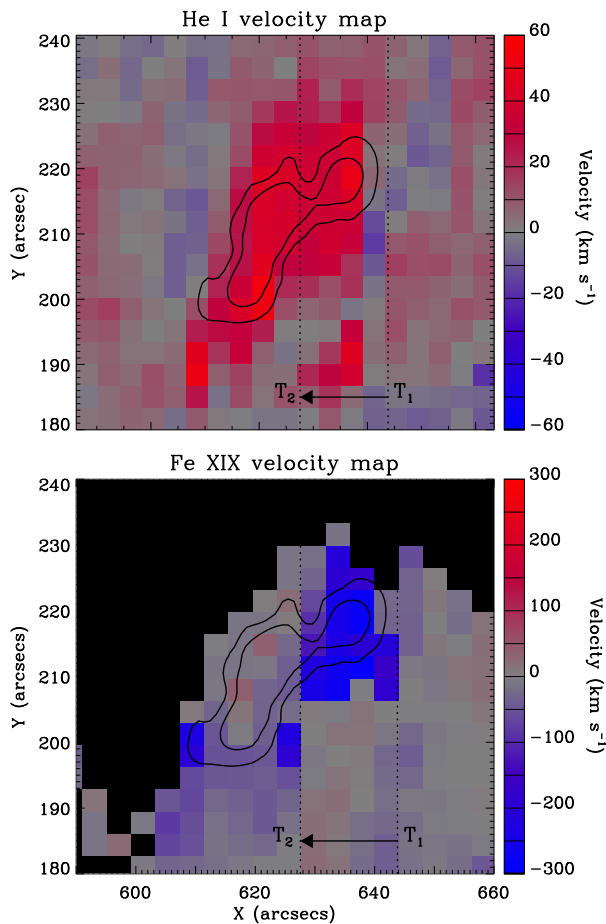


Fig. 4.— Velocity maps in He I and Fe XIX. Downflows are indicated by red pixels while upflows are indicated by blue pixels. The vertical *dashed* lines correspond to the times indicated by the vertical *dashed* lines in Figure 3 and the arrow denotes the direction in which the CDS slit moves. Black regions in the Fe XIX map represent pixels where no significant Fe XIX emission was observed. *RHESSI* 25–60 keV contours at 10% and 40% of the peak intensity are overlaid.

Figure 4 shows velocity maps in the He I and Fe XIX lines. The He I map shows consistent downflows of  $20\text{--}50\text{ km s}^{-1}$  until the slit leaves the flaring region at  $\sim 12:50$  UT. A velocity map in O V showed a similar trend. However, the Fe XIX map shows strong upflow velocities of  $190\text{--}280\text{ km s}^{-1}$  during the HXR peak, indicated by ‘T<sub>1</sub>’ and ‘T<sub>2</sub>’ on Figures 3 and 4. No significant

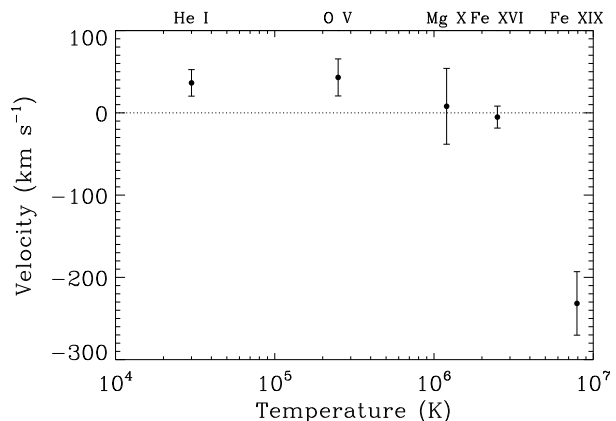


Fig. 5.— Plasma velocity as a function of temperature for the five lines observed using CDS. Positive velocities indicate downflows, while negative values indicate upflows.

upflows were evident once the HXRs begin to diminish from time T<sub>2</sub> onwards.

By identifying each pixel in the Fe XIX map that required a two-component fit to the line profile, between times T<sub>1</sub> and T<sub>2</sub>, the velocity was measured for the corresponding pixel in each of the five CDS rasters. Figure 5 shows the mean velocity as a function of temperature for each line using the methods described in Section 2. The error bars represent a  $1\sigma$  dispersion. At chromospheric and transition region temperatures, plasma velocities show red-shifts of  $36\pm 16\text{ km s}^{-1}$  and  $43\pm 22\text{ km s}^{-1}$ , respectively, while the blue-shift observed in the 8 MK Fe XIX line corresponds to a velocity of  $230\pm 38\text{ km s}^{-1}$ . No significant flows were observed in the Mg X and Fe XVI lines. The combination of high-velocity upflows and low-velocity downflows, together with a non-thermal electron flux of  $\geq 4\times 10^{10}\text{ ergs cm}^{-2}\text{ s}^{-1}$  provides clear evidence for explosive chromospheric evaporation.

#### 4. DISCUSSION AND CONCLUSIONS

For the first time, co-spatial and co-temporal HXR and EUV observations of chromospheric evaporation are presented using *RHESSI* and *SOHO*/CDS. High upflows velocities ( $\sim 230\text{ km s}^{-1}$ ) were clearly observed in high-temperature Fe XIX emission during the impulsive phase of an M2.2

flare, while much lower downflow velocities ( $\sim 40 \text{ km s}^{-1}$ ) were observed in the cooler He I and O V lines. The value of the non-thermal electron flux ( $\geq 4 \times 10^{10} \text{ ergs cm}^{-2} \text{ s}^{-1}$ ) and the resulting velocity response are indicative of an explosive evaporation process occurring during this flare, as laid out in Fisher, Canfield, & McClymont (1985a) and Mariska, Emslie, & Li (1989).

The combination of HXR and EUV observations presented in this *Letter* have enabled us to obtain a greater understanding of the characteristics of chromospheric evaporation, a fundamental process in solar flares. We have presented the first detection of explosive mass motions within HXR footpoints, and determined the flux of non-thermal electrons responsible for driving such flows.

This work has been supported by a Department of Employment and Learning (DEL) studentship and a Cooperative Award in Science and Technology (CAST). FPK is grateful to AWE Aldermaston for the award of a William Penny Fellowship. We would like to thank Drs. Brian Dennis, Joe Gurman, and Dominic Zarro at NASA Goddard Space Flight Center for their stimulating discussion and continued support. We would also like to thank the anonymous referee for their comments and suggestions which have greatly improved this *Letter*. SOHO is a project of international collaboration between the European Space Agency (ESA) and NASA.

## REFERENCES

- Antiochos, S. K., & Sturrock, P. A. 1978, *ApJ*, 220, 1137
- Antonucci, E., & Dennis, B. R. 1983, *Sol. Phys.*, 86, 67
- Brosius, J. W., & Phillips, K. J. H. 2004, *ApJ*, 613, 580
- Brown, J. C. 1971, *Sol. Phys.*, 18, 489
- Czaykowska, A., De Pontieu, B., Alexander, D., & Rank, G. 1999, *ApJ*, 521, L75
- Del Zanna, G., & Mason, H. E. 2005, *A&A*, 433, 731
- Del Zanna, G., Berlicki, A., Schmieder, B., & Mason, H. E. 2005, *Sol. Phys.*, *In Press*
- Delaboudinière, J. -P., et al. 1995, *Sol. Phys.*, 162, 291
- Fisher, G. H., Canfield, R. C., & McClymont, A. N. 1984, *ApJ*, 281, L79
- Fisher, G. H., Canfield, R. C., & McClymont, A. N. 1985a, *ApJ*, 289, 414
- Fisher, G. H., Canfield, R. C., & McClymont, A. N. 1985b, *ApJ*, 289, 425
- Fisher, G. H., Canfield, R. C., & McClymont, A. N. 1985c, *ApJ*, 289, 434
- Harrison, R. A., et al. 1995, *Sol. Phys.*, 162, 233
- Holman, G. D. 2003, *ApJ*, 586, 606
- Hurford, G. J., et al. 2002, *Sol. Phys.*, 210, 61
- Lin, R. P., et al. 2002, *Sol. Phys.*, 210, 3
- Mariska, J. T., Emslie, A., G., & Li, P. 1989, *ApJ*, 341, 1067
- Phillips, K. J. H. 2004, *ApJ*, 605, 921
- Sui, L., Holman, G. D., & Dennis, B. R. 2005, *ApJ*, 626, 1102
- Teriaca, L., Falchi, A., Cauzzi, G., Falciani, R., Smaldone, L. A., & Andretta, V. 2003, *ApJ*, 588, 596
- Thompson, W. T. 1999, CDS Software Note No. 53
- Veronig, A. M., Brown, J. C., Dennis, B. R., Schwartz, R. A., Sui, L., & Tolbert, A. K. 2005, *ApJ*, 621, 482
- Zarro, D. M., & Lemen, J. R. 1988, *ApJ*, 329, 456